Hydraulic fracturing: Laboratory evidence of the brittle-to-ductile transition with depth

Runhua Feng[1*], Shuo Liu[1] , Joel Sarout[2] , Jeremie Dautriat[2], Zhiqi Zhong[1,3], Reza Rezaee[1], Mohammad Sarmadivaleh[1*]

[1]School of WASM: Minerals, Energy and Chemical Engineering, Curtin University, 26 Dick Perry Ave, Kensington, WA 6151 Australia

[2]CSIRO Energy, Perth, WA 6151, Australia

[3] College of Energy, Chengdu University of Technology, Chengdu, China

*Corresponding author:

E-mail address: runhua.feng@student.curtin.edu.au (R.Feng); mohammad.sarmadivaleh@curtin.edu.au (M.Sarmadivaleh)

Highlights:

- Hydraulic fracturing experiments are conducted on artificial geomaterials exhibiting a wide range of rheology subjected to true triaxial stresses with a low (σ_v = 6.5 MPa, σ_H =3 MPa, and σ_h =1.5MPa), and a higher (15 MPa, 10 MPa, and 5MPa) confinement.
- The intermediate stress plays a profound role in hydraulic fracture (HF) propagation i.e., the transition of intermediate strain are observed from brittle to ductile samples.
- The transitional high-to-low inclined angle of hydraulic fracture are observed from brittle/semi-brittle samples to semi-ductile/ductile samples, due to the plastic yielding/stress softening near the fracture tip.
- The surface area of the hydraulic fractures is shown to be reduced when transiting from the brittle to the ductile regime.

Abstract

Understand the propagation of hydraulic fracture (HF) is essential for effectively stimulating the hydrocarbon production of unconventional reservoirs. Hydraulic fracturing may induce distinct failure modes within the formation, depending on the rheology of the solid and the *in-situ* stresses. A brittle-to-ductile transition of HF is thus anticipated with increasing depth, although only scarce data are available to support this hypothesis. Here we carry out laboratory hydraulic fracturing experiments in artificial geomaterials exhibiting a wide range of rheology: cubic samples 50x50x50 mm^3 in size are subjected to true triaxial stresses with either a low (σ_v = 6.5 MPa, σ_H =3 MPa, and σ_h =1.5MPa), or a high (15 MPa, 10 MPa, and 5MPa) confinement. The 3D strains induced by hydraulic fracturing are monitored and interpreted; and X-ray Computed Tomography (CT) imaging is used to document the HF geometry. Finally, a correlation between the normalized fracture area (A_{FN}) and the brittleness index (BI) of tested samples is introduced. Our results reveal that: (i)The intermediate stress plays a profound role in hydraulic fracture propagation subjected to the designed stress regimes (i.e., the transitional intermediate strain observed from brittle to ductile samples); (ii) The transitional inclined angle (high-to-low) of HFs are observed from brittle/semi-brittle samples to semi-ductile/ductile samples; (iii) The normalized fracture area (A_{FN}) is shown to be larger when the BI is higher; the A_{FN}, tortuosity and roughness of the HF are shown to be larger as the increase of confinement.

Keywords: Hydraulic fracture propagation; Geometry of hydraulic fractures; Brittle-to-ductile transition; Fractured area; True triaxial stresses

1. Introduction

The deformation of geo-materials incorporate the process as shear stress is increased toward failure: I- initial elastic deformation; II – non-recoverable deformation, i.e., brittle micro-cracking, or ductile/plastic flow; III – micro-cracks nucleation and macroscopic fracture propagation. The three stages are highly influenced by the confinement of stress, a brittle-to-ductile transitional failure is thus expected and observed as the increase of confinement (Evans et al. 1990; Zhang et al. 1993; Nygård et al. 2006; Wong and Baud 2012; Minaeian 2014; Vachaparampil and Ghassemi 2017; Aharonov and Scholz 2019). However, much fewer studies focus on the transitional deformation induced by hydraulic fracturing emerging in a wide range of underground engineering applications. Hydro-mechanical force is the main driven mechanism for the propagation of hydraulic fracture and with the same analogy, such transitional failure should be a measurable function of stress. Deeply understanding this

transitional deformation can facilitate not only theoretical/numerical modelling but also provide critical insights for field applications associated with hydraulic fracturing.

When hydraulic fracture initiates and propagates within geo-materials under *in-situ* stresses, three types of failure modes are often observed: mode-I (tensile), mode-II (shear), and mixed-mode-I and II (Economides and Nolte 1989; Gischig and Preisig 2015; Wu 2006). The stress anisotropy, fluid mechanics, natural fractures, and rock mechanical properties are recognized as the most influential factors in the failure mode (Papanastasiou 1997; Zhou et al. 2008; Zhang et al. 2009; Sarmadivaleh 2012; Wang et al. 2013; Gischig and Preisig 2015; Wang 2019; Li et al. 2020; Liu et al. 2020; Zeng et al. 2020; Yang et al. 2021). Incorporating all these parameters in fracturing analysis is complicated to be achieved. Since the hydraulic fracture growth is a dynamic process where the damage is mainly accumulated adjacent to the tip within the process zone (Desroches et al. 1994; ; Papanastasiou 1997; Elices et al. 2002; Garagash 2019; Ju et al. 2021; Liu and Lecampion 2021), which allows an alternative way studying the fracturing process. Several studies demonstrated that the plastic yielding/stress softening at the tip will absorb the effective injection energy, which significantly hinders the fracture propagation and results in a uniformed fracture geometry in ductile rocks (Papanastasiou 1997; Feng et al. 2020; Ju et al. 2021; Parisio et al. 2021). Recently, Ju et al. (2021) performed a 3D numerical model for hydraulic fracture propagation in tightly brittle and ductile reservoirs. They confirmed that the stress concentration near the fracture tip is highly accommodated in the ductile reservoir. Parisio et al. (2021) carried out an experimental study of the brittle-to-ductile transition of hydraulic fracture within Polymethyl Methacrylate (PMMA). They observed complex fracture patterns under non-uniform stress distribution in the sample under the brittle regime. The complexity of fracture is significantly reduced as the ductility is increased. These studies revealed that a brittle-to-ductile transition is anticipated for the hydraulic fracture in a wide range of rocks types in elevated confinements. However, such experimental study on a wide range of geo-materials is still lacking, which is essential to provide enough data set required for the calibration of the modelling suitable for field applications.

In this paper, we present hydro-mechanical data based on hydraulic fracturing tests on variable types of geomaterials subjected to two sets of true triaxial stress conditions (TTSC), i.e., low confining (σ_1= 6.5MPa, σ_2= 3MPa, and σ_3=1.5MPa), and higher confining stresses (σ_1= 15MPa, σ_2=10MPa, and σ_2=5MPa); the evolution of wellbore pressure and the three mutually orthogonal strains induced by hydraulic fracture propagation are intepreted. We also

interpreted the geometry and surface area (A_F) of hydraulic fracture based on the visualisation of the X-ray Computational Tomography (CT) images of tested samples. These quantifications allow us to correlate the A_F and the brittleness index (BI) of the samples subjected to hydraulic fracturing; this correlation is compared against the previous numerical study.

2. Theory

2.1 Propagation Criterion for Hydraulic Fracture

Stress intensity factor (K) at the crack tip has been studied as an important parameter in linear elastic fracture mechanics (Irwin 1957). Later, Barenblatt (1962) and Dugdale (1960) proposed a well-known Barenblatt-Dugdale model, accounting for the nonlinear material behaviour into a small size of cohesive zone near the crack tip. Hillerborg et al. (1976) introduced a model for the finite cohesive zone, adapting to the propagation of a cohesive crack in elastic material when the tensile softening takes place (Boone et al. 1986; Papanastasiou and Thiercelin 1993; Desroches et al. 1994).

For propagating a penny-shaped hydraulic fracture (**Fig.1**), the three aspects- (i) fluid pressure, (ii) *in-situ* stresses, and (iii) cohesive stresses are necessarily considered into the stress intensity factor (K_{HF}) (Lhomme 2005). The pressurized fracturing fluid provides a positive contribution to the stress intensity factor $K_I(P_f)$ reads:

$$K_I(P_f) = 2\sqrt{\frac{R}{\pi}}\int_0^{c_f} K_{np}(\xi, c)p_f(\xi, t)d\xi \tag{1}$$

Where P_f is the fluid pressure, R is the radius of fracture extent, R_f is the radius of fluid front (**Fig.1**); $\xi = x/R_w$, $c = R/R_w$, and $c_f = R_f/R_w$ are the normalized length variables to borehole radius R_w; the kernel function $K_{np}(\xi, c)$ denotes the effect of wellbore geometry in stress intensity factor(Keer et al. 1977; Nilson and Proffer 1984; Lhomme 2005).

If we consider a hydraulic fracture subjected to the both horizontal stresses, i.e., minimum (σ_h) and intermediate (σ_H), the resultant normal stress on the fracture walls (σ_r) negatively contributed to the stress intensity factor $K_I(\sigma_r)$ reads:

$$K_I(\sigma_r) = -2\sqrt{\frac{R}{\pi}}\sigma_r\int_0^{c} K_{np}(\xi, c)d\xi \tag{2}$$

The inelastic behaviour can be modelled by tensile cohesive stresses exerted on the fracture wall within the cohesive zone (Elices et al. 2002; Lhomme 2005; Garagash 2019; Liu and Lecampion 2021), a degradation function f_{wct} is introduced to address the linear/nonlinear

relation between the cohesive stress (σ_{coh}) and associated fracture opening (w) from the peak load to critical fracture opening (w_c):

$$\sigma_{coh} = \sigma_t f_{w_{ct}}, \ 0 < f_{w_{ct}} < 1, \ w < w_c \quad (3)$$

$$\sigma_{coh} = 0, \ w \geq w_c \quad (4)$$

The cohesive stresses provided a negative contribution to the stress intensity factor $K_I(\sigma_{coh})$ reads as:

$$K_I(\sigma_{coh}) = -2\sqrt{\frac{R}{\pi}}\sigma_t \int_{c_v}^{c} K_{np}(\xi, c) f_{w_{ct}} d\xi \quad (5)$$

Where R_v is the visible radius of the crack (**Fig.1**); $c_v = (R_v - R_w)/ R_w$

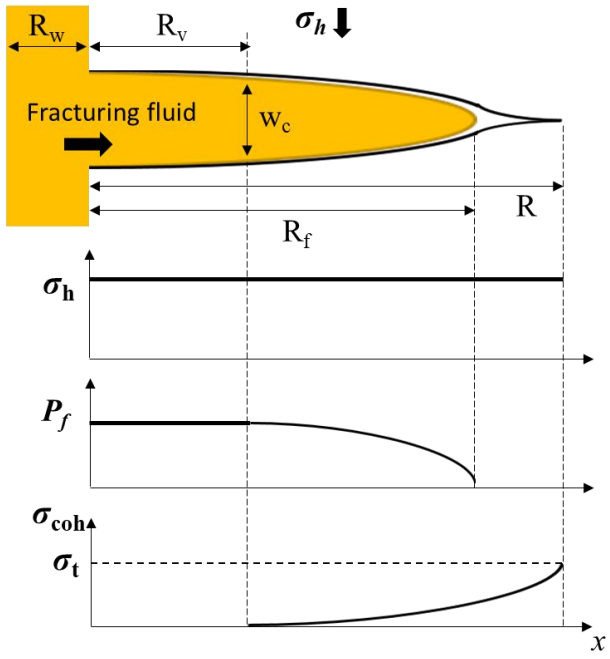

Fig.1 Schematic of loading of a penny-shaped hydraulic fracture with fluid lag (Image modified from Lhomme (2005))

2.2 Propagation Condition

The summation of the three contributions (**Eqs.1 to 3**) to the stress intensity factor (K_{HF}) for hydraulic fracture is necessarily to be equal to zero at the true crack tip, reads:

$$K_{HF} = K_I(P_f) + K_I(\sigma_r) + K_I(\sigma_{coh}) = 0 \quad (6)$$

In order to propagate a hydraulic fracture, the K_{HF} must be larger than 0, reads:

$$\underbrace{2\sqrt{\frac{R}{\pi}}\int_0^{c_f} K_{np}(\xi,c)p_f(\xi,t)d\xi}_{K_I(P_f)} > \left[\underbrace{2\sqrt{\frac{R}{\pi}}\sigma_r\int_0^{c} K_{np}(\xi,c)d\xi}_{K_I(\sigma_r)} + \underbrace{2\sqrt{\frac{R}{\pi}}\sigma_t\int_{c_v}^{c} K_{np}(\xi,c)f_{w_{ct}}d\xi}_{K_I(\sigma_{coh})}\right] \quad (7)$$

and reduces to:

$$\int_0^{c_f} K_{np}(\xi,c)p_f(\xi,t)d\xi > \left[\sigma_r\int_0^{c} K_{np}(\xi,c)d\xi + \sigma_t\int_{c_v}^{c} K_{np}(\xi,c)f_{w_{ct}}d\xi\right] \quad (8)$$

It can be seen that both σ_r and σ_{coh} provide the resistance for initiation and propagation of a hydraulic fracture (HF). It is worthy to note that the intermediate stress σ_H may play an important role in K_I (σ_r) if the HF is inclined to the directions of both horizontal stresses. Therefore, the performance of σ_H and the intermediate strain ε_H induced by HF propagation are worthily to be monitored/evaluated (see **Section 4.2 or Appendix.B**). The cohesive stress σ_{coh} profoundly affect the propagation of a HF, especially for soft/ductile materials under stress field (Papanastasiou and Thiercelin 1993; Papanastasiou 1997; Ju et al. 2021; Liu and Lecampion 2021). If the different materials exhibit the same value of both K_I (P_f) and K_I (σ_r), the K_I (σ_{coh}) will be the dominated parameter differentiating the behaviour of fracture propagation.

3. Experimental Procedure

The six types of samples (see details of sample preparation and rock characterization in **Appendix A**) are used for hydraulic fracturing experiments under true triaxial stress conditions. Honey is used as fracturing fluid due to its Newtonian behaviour. A micro-metering needle valve V_i is added to the injection inlet to restrict the flow rate when the rock breakdown takes place (Bunger 2005; Sarmadivaleh 2012). The experiments consist of three main components (**a**-pumping system; **b**-fracturing system **c**-data acquisition system) and are conducted in the following steps (**Fig.2)**:

(i) The cubic samples are initially loaded into the cell (**Fig.2b**), where the injection tube glued into the wellbore is connected to the injection line of the fracturing fluid.

(ii) The confining stresses are simultaneously elevated to a target value (all stresses elevated to minimum stress, then two bigger stresses raised to the intermediate level, finally, the maximum stress is reached on one side)**,** i.e., the loading rate is sufficiently small and constant to avoid any premature cracks induced by stresses. Waiting for at least 12hrs to ensure the stresses reach an equilibrium state.

(iii) Vacuuming the injection line before injecting the honey into the wellbore (**Fig.2a**); monitoring the wellbore pressure for 1 hr when it reached a constant vacuum pressure value of -14 psi.

(iv) Start to inject the fracturing fluid into wellbore; adjust the valve V_i to a consistent value (V_i is set to 2/7 open for the tests under low confinement i.e., $\sigma_v = 6.5$ MPa, $\sigma_H = 3$ MPa, $\sigma_h = 1.5$ MPa, , but 3/7 open for the high confinement i.e., $\sigma_v = 15$ MPa, $\sigma_H = 10$ MPa, $\sigma_h = 5$ MPa); start to monitor the wellbore pressure and strain at the same time.

After the fracturing tests are completed, all samples are scanned a 3D X-ray Computed Tomography (XCT) images at a voxel resolution of 0.1 x 0.1 x 0.1 mm (Siemens SOMATOM Definition AS, set for helical scanning at 140 kV/500 mA) were produced to document the geometry of hydraulic fractures within the samples. All quantities from CT images are interpreted by Avizo software (Liu et al. 2022).

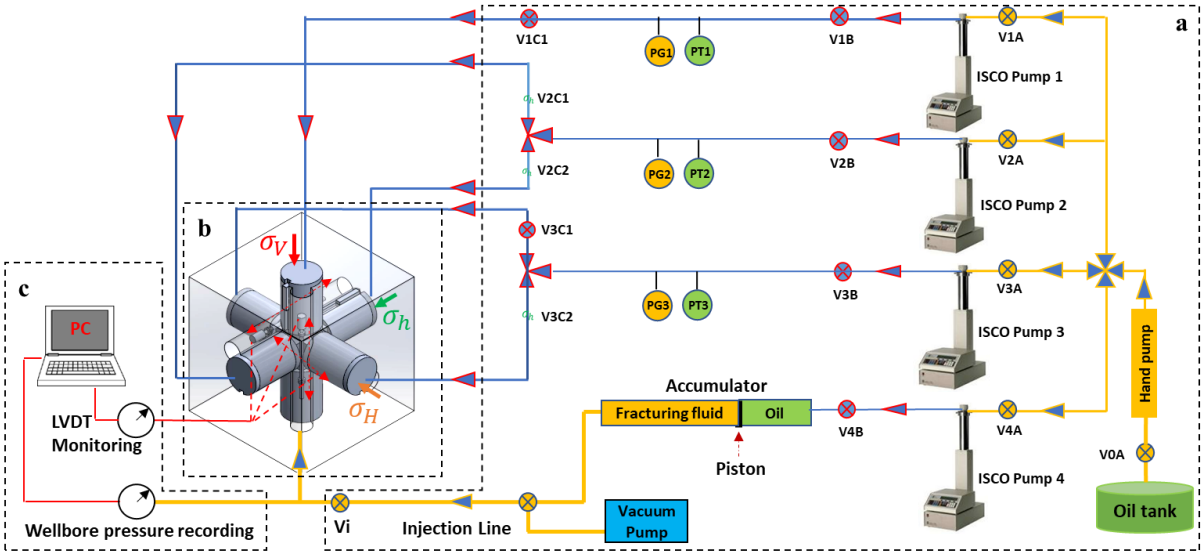

Fig.2 Schematic of hydraulic fracturing experimental setup: **a** Pumping system; **b** fracturing system; and **c** data acquisition system. *PT* pressure transducer, *PG* pressure gauge, V valve, Vi micro-meter valve, LVDT Linear Variable Differential Transformer, PC data acquisition.

4. Results

According to the recent study by Feng et al (2022), the six types of samples are classified as brittle PMMA (BI=0.99), semi-brittle rock S_1 (BI=0.66), semi-brittle rock S_4 (BI=0.57), semi-ductile rock S_3 (BI=0.46), the ductile rock S_5 (BI=0.38) and S_2 (BI=0.31) under the low confinement. The same classification but different BI values under higher confinement: PMMA (BI=0.87), S_1 (BI=0.36), S_4 (BI=0.28), S_3 (BI=0.2), S_5 (BI=0.15), and S_2 (BI=0.12). The hydromechanical results for semi-brittle (S_1) and ductile rocks (S_2) under low and high

confinement are presented in **Section 4.1**; the full data set (PMMA, and rock samples from S_1 to S_5) can be found in **Appendix B**. We also discuss the characteristics of intermediate strain (ε_H) induced by hydraulic fracture propagation (**Section 4.2**). Moreover, the geometry of hydraulic fracture under both confinements are presented (**Section 4.3**). Finally, the correlation between fractured area and brittleness index (BI) is studied in **Section 4.4**.

4.1 Hydromechanical data

Figure 3 shows the representative hydro-mechanical data (the wellbore pressure and 3D strain induced by hydraulic fracture) during the hydraulic fracturing for semi-brittle (S_1) and ductile samples (S_2) under low (**Fig.3a and b)** and high (**Fig.3c and d)** confinement stresses. The minimum horizontal strain ε_h is induced by the initiation and propagation of the fracture (negative ε_h in green), whereas the positive vertical strain ε_V (blue curve) indicates the vertical contraction induced by the vertical stress. The full data set of tested samples are presented in **Appendix.B**.

From formation breakdown (maximum wellbore pressure) until the pressure reaches to the constant propagation pressure, for semi-brittle rock S_1 the acceleration of wellbore pressure drop occupies the major portion; however, for ductile samples (S_5 and S_2), the acceleration only occupies a small portion, but it quickly shifts to deceleration during the entire process. Notably, for both samples under higher confinement, the depressurization is significantly decelerated comparing to that of lower confinement.

It can be seen that the negative minimum horizontal strain ε_h is induced by the hydraulic fracture opening and propagating, whereas the positive vertical strain ε_V is induced by the vertical compressive stress σ_V during fracture propagation. For semi-brittle rock S_1, after breakdown the strain ε_h abruptly increases (**Fig.3a and c**) comparing to ductile rock S_2 where the ε_h increases gradually to the peak value (**Fig.3b and d**). Furthermore, it revealed that the magnitude of strain ε_H along the intermediate horizontal stress σ_H (orange curve) show slightly negative deflection (tension) for semi-brittle sample S_1 under both low (**Fig.3a**) and high confinement (**Fig.3c)**; slightly positive deflection (compression) for ductile sample S_2 under low confinement(**Fig.3b**); but a significant positive deflection (compression) of ε_H is observed for S_2 under high confinement (**Fig.3d**). The more details regarding to the characteristics of intermediate strain ε_H are presented in **Section 4.2**

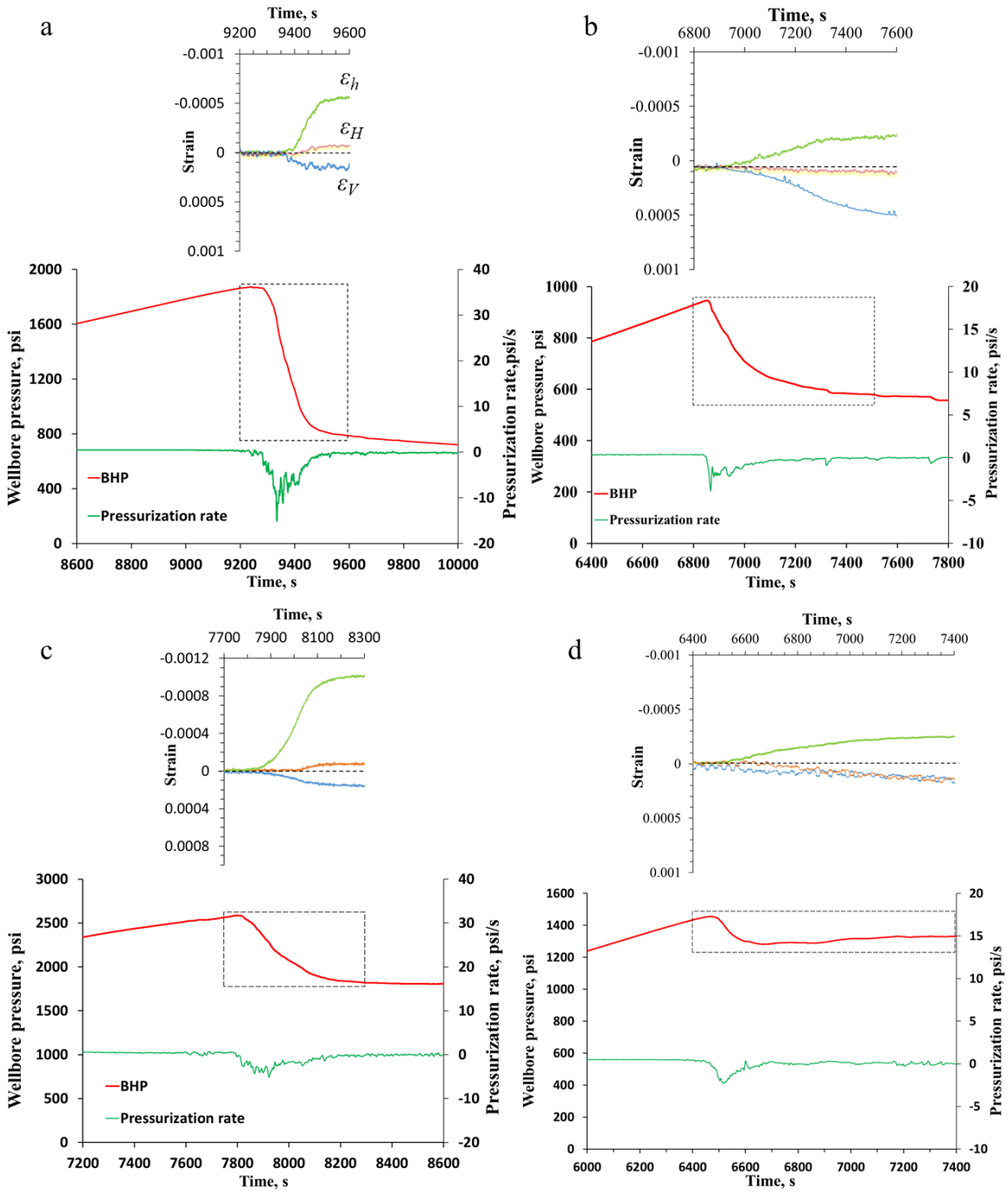

Fig.3 Representative synchronization of wellbore pressure and hydraulic fracture induced strain under low confinement-6.5MPa , 3MPa, and 1.5MPa: a) S_1 b) S_2; and high confinement-15MPa , 10MPa, and 5MPa: c) S_1 d) S_2

4.2 Intermediate strain (ε_H) transition

Refer to the full hydro-mechanical data set (**Appendix B**), the vertical strain ε_v shows a compression, and the minimum horizontal strain ε_h exhibits tension for all samples. However, the characteristics of intermediate strain ε_H are highly variable (depend on the sample types and confinement) (**Fig.4**). For semi-ductile S_3, and ductile samples S_5 and S_2 under higher

confinement (**Fig.4b**), the magnitude of ε_H is significantly larger than that of lower confinement (**Fig.4a**). In summary, the significant transitions of ε_H from the brittle to ductile samples are observed:

Under the low confinement (**Fig.4a**): the intermediate strain ε_H shows a significant tensile deflection for brittle PMMA; a moderate tensile deflection for semi-brittle rock sample S_1 and S_4; a slight deflection for semi-ductile S_3; a nearly constant ε_H for ductile S_5; while a slight compressive deflection for ductile rock sample S_2.

Under the high confinement (**Fig.4b**), the transition is analogous to the lower one: the negative deflection of ε_H becomes ease for PMMA, and still exhibits the highest value among all samples; for the rock samples (from S_1 to S_5), the moderate negative deflection of ε_H are observed in semi-brittle rock sample S_1 and S_4 , but a significant positive compression of ε_H are found in semi-ductile S_3 , ductile S_5 and S_2.

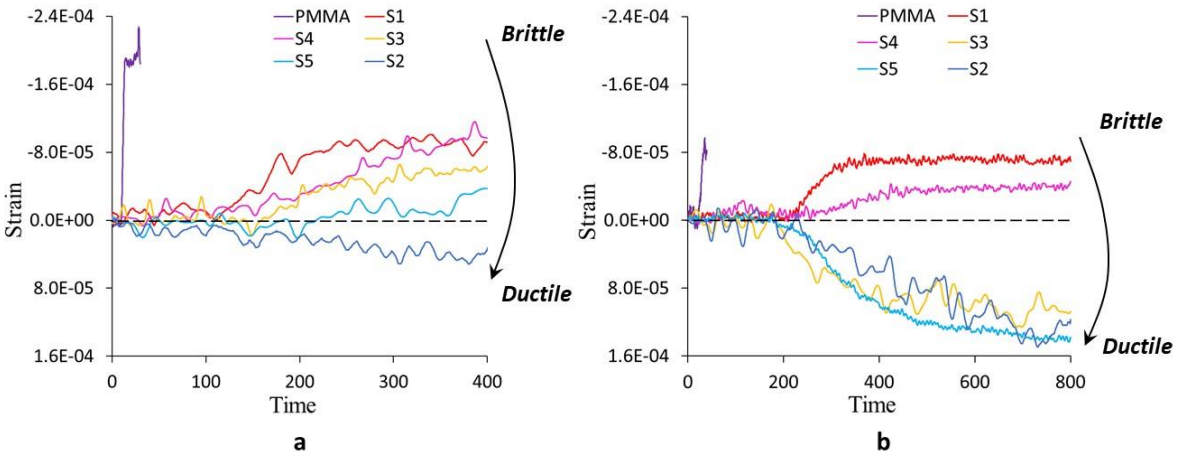

Fig.4 Transition of intermediate strain ε_H from brittle to ductile samples for a) low confinement b) high confinement

4.3 Geometry

The geometry of hydraulic fracture for different samples subjected to low confinement (i.e., 6.5, 3 , and 1.5MPa) are shown in **Fig.5**. The fractures are highly tilted with respect to both σ_H and σ_h for brittle PMMA (**Fig.5a)**, and semi-brittle rock S_1 **(Fig.5b)** and S_4 **(Fig.5c)**. For the semi-ductile S_3(**Fig.5d**) and ductile rock S_5 (**Fig.5e**), the tilted angle are significantly reduced. In contrast, for ductile sample S_2 the fractures are nearly orthogonal to σ_h only (**Fig.5f**). Overall, it turns out a clear transition from highly titled (brittle) to orthogonal (ductile) fractures as the increase of ductility. This analogous phenomenon is also observed in the samples subjected to higher confinement (i.e., 15, 10 , and 5MPa) (**Fig.6**). The most interesting observation is the significant shear failure induced by hydraulic fracturing within PMMA: the geometry of

hydraulic fracture (HF) is highly titled to ε_V and ε_h (**Fig.6a**), instead of inclining to ε_H and ε_h subjected to the lower confinement. Macroscopically, the geometry of hydraulic fractures are more planar/smooth under high confinement (**Fig.6**) rather than that of relatively tortuous fractures under the low confinement (**Fig.5**).

The experimental geometry of hydraulic fracture(HF) with respect to the brittle and ductile rocks (**Figs.5 and 6**) are in good agreement with the numerical study performed by Ju et al. (2021): for brittle reservoir the fracture is severely titled and result in a nonplanar geometry (**Fig.7a**), while for the ductile reservoir the inclination of fracture is highly mitigated due to the tip plasticity (**Fig.7c**), resulting in an axisymmetrically short fracture. Their numerical results are shown to be more consistent with our experimental geometry of HF subjected to the high confinement (**Fig.6**).

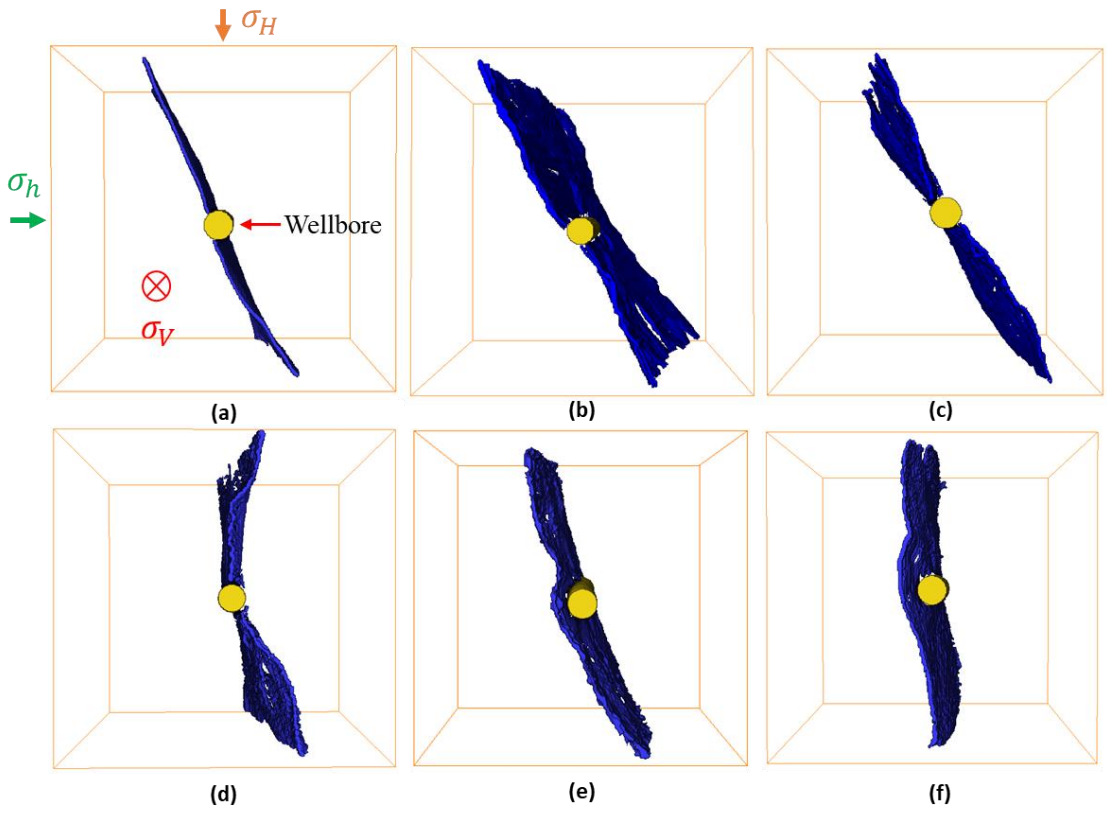

Fig.5. Geometry of hydraulic fracture from brittle to ductile transition a) PMMA b) S_1 c) S_4 d) S_3 e) S_5 f) S_2 under 6.5, 3.0, 1.5MPa

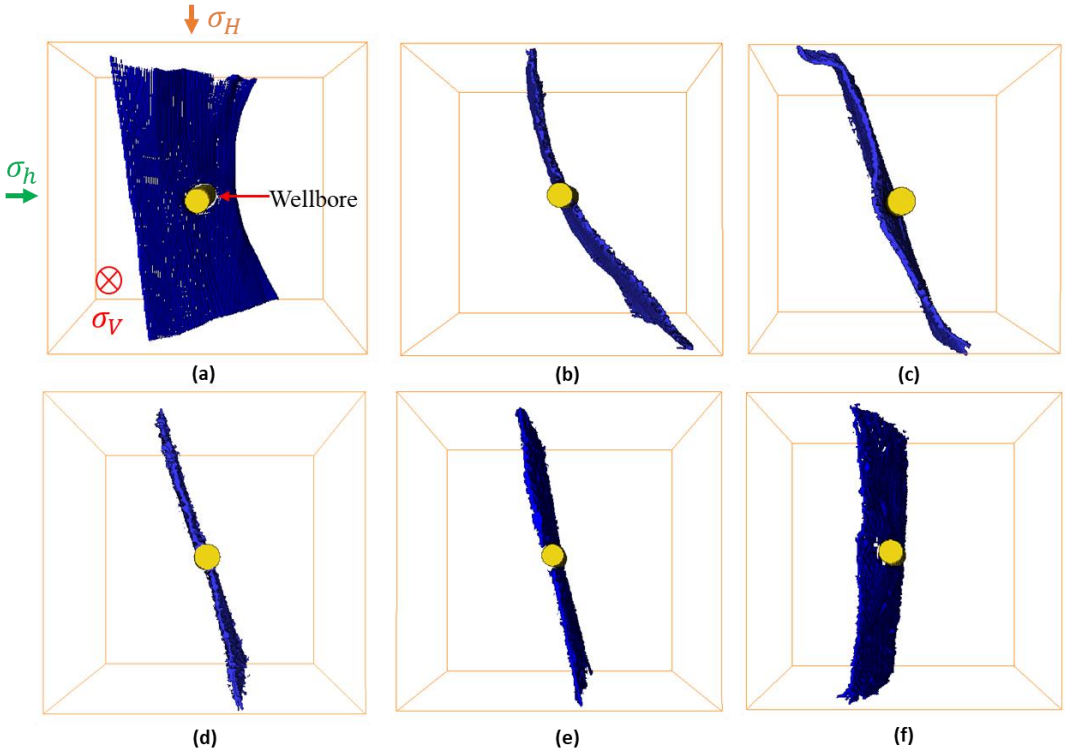

Fig.6. Geometry of hydraulic fracture from brittle to ductile transition a) PMMA b) S_1 c) S_4 d) S_3 e) S_5 f) S_2 under 15, 10, 5MPa

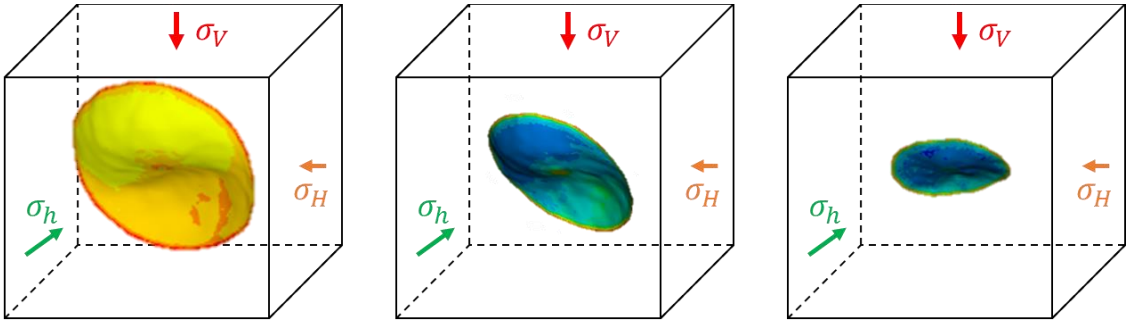

Fig.7. Numerical modelling of the morphology of hydraulic fracture from a) brittle, b) semi-brittle, and c) ductile reservoir under true triaxial stresses σ_v=30MPa, σ_H= σ_h=20MPa. Images modified from a 3D numerical work (Ju et al. (2021)).

4.4 Fractured area vs BI

Ju et al. (2021) numerically studied the relation between fractured area and the brittleness index (BI) of shale reservoir. He showed that the fractured area is increased as the increase of BI. Here we quantify the hydraulic fractured area based on the CT images of tested rock samples (S_1 to S_5). We normalized the numerical (A_{TN}) and experimental fractured area (A_{FN}), and plot both A_{TN} and A_{FN} verse BI (**Fig.8**). Both A_{FN} and A_{FN} show an increased trend as the increase of BI. Notably, under the low confinement, the fitting of A_{FN} and BI shows a second polynomial relation (**Fig.8b**), which is different from the linear fitting between A_{TN} and BI (**Fig.8a**). On

the other hand, under the high confinement (**Fig.8b**), the analogous second polynomial relation (coefficients) are observed for both A_{FN} and A_{TN} verse BI; but their quantities are significantly different.

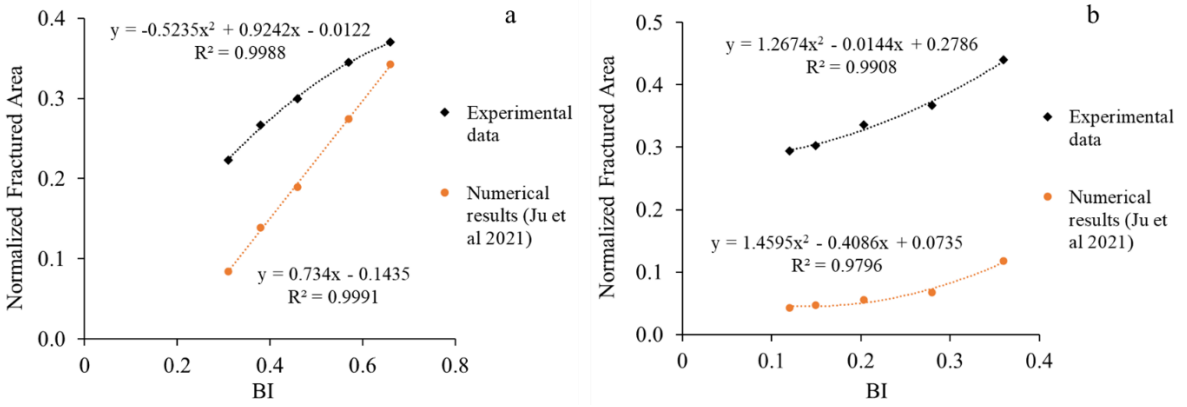

Fig.8 Normalized fractured area vs brittleness index (BI) based on our experimental results under a) low and b) high confinement, and the literature data

5. Discussion and implementations

5.1 hydraulic fracture induced failure from low to high confinement

Under the lower confinement, the failure of brittle PMMA(**Fig.B1a**) and the semi-brittle rock S_1 (**Fig.B1b**) are localized (i.e., tensile-shear opening mode caused by the differential stresses). On the other hand, the nonlocalized deformation are mainly observed in semi-brittle S_4 (**Fig.B1c**), semi-ductile S_3 (**Fig.B1d**), and ductile rocks S_5 (**Fig.B1e**) and S_2 (**Fig.B1f**). Such deformation is evidenced by the associated vertical strain ε_V in a strongly compressive manner, which is also observed and evidenced by the spatial extend deformation (nonlocalized strain) induced by ductile failure in glass (Richard et al. 2021).

For higher confinement, the failure of PMMA(**Fig.B2a**) and the semi-brittle rock S_1(**Fig.B2b**) are still dominated by the localized deformation, either in vertical shear dilation (PMMA) or lateral shear-tensile opening (S_1). However, the nonlocalized deformation are enhanced in semi-brittle (S_4), semi-ductile (S_3), and ductile rocks (S_2 and S_5), which are evidenced by the suppressed ε_H and significantly compressive ε_V associated with hydraulic fracture propagation in S_4 (**Fig. B2c**); and strongly compressive ε_H and ε_V in S_3 (**Fig. B2d**), S_5 (**Fig. B2e**), and S_2 (**Fig. B2f**). Specifically, for each type of sample under both low and high confinement:

(i) For brittle PMMA subjected to low confinement, the failure mode is lateral tensile-shear opening (**Fig.B1a**), but it becomes tensile-shearing (vertical) under high confinement (**Fig.B2a**): the significantly incremental vertical strain ε_v and observed geometry (**Fig.6a**) indicate that the hydraulic fracture initiation/propagation induce the vertical shear failure

mainly followed to the fictitious failure plane (**Fig.10**), attributing to the high stress concentration near the fracture tip (higher K_{HF}). Unlike the maximum horizontal strain ε_H which is comparable to the minimum horizontal ε_h at low confinement, the ε_H is negligible comparing to the vertical ε_v and minimum horizontal strain ε_h under the high confinement.

(ii) For the semi-brittle rock (S_1), the failure modes are dominated by the localized tensile-shear opening subjected to lateral direction under both low and high confinement (**Figs.B1b and B2b**). The 3D strain induced by hydraulic fracture are qualitatively consistent for both low (**Fig.B1b)** and high (**Fig.B2b)** confinement; while the minimum horizontal strain ε_h under the higher confinement is significantly higher than that of lower one, which is attributed to the significantly higher breakdown and propagation pressure (higher K_I (P_f)).

(iii) For semi-brittle rock (S_4) the negative deflection of ε_H is highly suppressed under high confinement (**Fig.B2c**), attributing to the higher ductility/nonlocalized deformation. Although the breakdown pressure under higher confinement is almost double of the lower case, the ε_h is smoothly developed and the magnitude of ε_h is nearly the same as the lower one, which is attributed to the highly nonlocalized strain softening during fracture propagation (higher K_I (σ_{coh})).

(iv) For semi-ductile rock S_3 from low confinement (**Fig. B1d**) to high confinement (**Fig. B2d**), the maximum lateral strain ε_H is transited from tensile deflection (negative ε_H) to compressive deflection (postive ε_H). This can be explained by the highly increased ductility of S_3 (higher K_I (σ_{coh})) under higher confinement (higher K_I (σ_r)).

(v) For ductile rocks S_2 (**Fig. B2e**) and S_5 (**Fig. B2f**) under high confinement, the magnitude of ε_v are less than fifty percent of that of low confinement (**Figs. B1e and f**), notably, the ε_H is significantly compressed and nearly coincided with ε_v. This can be explained by the strongly nonlocalized deformation induced by strain softening (higher K_I (σ_{coh})) during the hydraulic fracture propagation.

5.2 Role of intermediate stress (σ_H) in hydraulic fracture

The intermediate stress σ_H is analytically proved as an important parameter in the stress intensity factor (K_{HF}) (**Eqs.6 to 8**) if the geometry of hydraulic fracture (HF) is inclined to directions of both horizontal stresses, which is often observed in the laboratory or field. Such experimental study are carried out to demonstrate the significant role of σ_H in the mechanical properties, and associated failure mode induced by elevated stresses on sandstone and shale

(Minaeian 2014). In this study, the intermediate strain ε_H induced by coupled hydraulic and mechanical force are highly variable regarding to the sample types. The deflection of ε_H exhibits a clear brittle-to-ductile transition among the tested samples for both low and high confinement (**Fig.4**). Noteworthily, for semi-ductile/ductile samples under the higher confinement, the ε_H becomes significantly compression at early stage after borehole failure. This is because the higher amount of injection energy is disspated within the cohesive stress (profound K_I (σ_{coh}) in **Eq.7**), causing more positive K_I (P_f) required to compensate the both negative K_I (σ_r) and K_I (σ_{coh}), resulting in the compressive ε_H. The significant cohesive stresses (σ_{coh}) due to nonlocalized plastic deformation at the fracture tip is also observed in such numerical studies (Papanastasiou 1997; Ju et al. 2021).

5.3 Geometry of hydraulic fracture

The representative transitional geometry of hydraulic fracture with respect to brittle and ductile rocks **(Figs.5 and 6)** are in good agreement with the numerical study **(Fig.7)** performed by Ju et al. (2021). **Fig.9** shows a typical shear failure induced by true tri-axial stresses compression (TTSC) i.e., $\sigma_v > \sigma_H > \sigma_h$ (Minaeian 2014; Rahjoo and Eberhardt 2021). Prior to this failure, assume a fictitious weak plane (normal faulting regime) is formed within the sample subjected to the stresses (**Fig.9**). Noteworthily, the fictitious weak plane is different from the weakest plane for propagation of a hydraulic fracture (i.e., the one perpendicular to minimum horizontal stress). Based on the geometry observed in our tested samples **(Figs.5 and 6)**, the representative schematic of brittle to ductile transition for the hydraulic fracture (HF) subjected to the designed stress regime are displayed in **Fig.10**.

Under the higher confininement: for HF initiates and reaches to breakdown pressure within brittle PMMA, due to the extremely high stress concentration near the crack tip, the highly effective propagation energy converted from pressurized fracturing fluid (higher K_I (P_f)) will drive the fracture propagating highly along to the normal faulting regime (see **Fig.9, Fig.10a, and Fig.B2a**), without being significantly affected by the stress redistribution. For semi-brittle rocks S_1 and S_4, the high stress concentration near the fracture tip is mitigated due to the strain softening (K_I (σ_{coh})), causing the vertical shearing failure appears to be highly eased **(Fig.10b**), instead, the hydraulic fracture is inclinded to intermediate stress σ_H due to stress redistribution. Subjected to low confinement, the alleviation of stress concentration near tip is also observed in the PMMA, in which the geometry of HF is analogous to the semi-brittle rocks S_1 and S_4.

Moreover, for semi-ductile sample (S_3), and ductile rocks (S_5 and S_2) subjected to the higher confinement: (i) the significant tip plasticity and softening behaviour (Papanastasiou 1997; Feng et al. 2020; Ju et al. 2021) highly reduce the stress concentration, which significantly reduces the kinematic energy transformation from the accumulated injection energy (lower K_{HF}). (ii) The reduction of effective propagation energy allow the stress redistributed on the samples. These mechanisms explain the geometry of hydraulic fracture always propagated along the weakest plane in semi-ductile/ductile samples, i.e., nearly perpendicular to the minimum horizontal stress **(Fig.10c or d)**, without being significantly affected by the fictitious weak plane induced by the deviatoric stress state ($\sigma_V > \sigma_H > \sigma_h$) shown in **Fig.9**. Notably, for the rock-like materials (S_1 to S_5) , the macroscopic geometry of hydraulic fractures subjected to high confinement **(Fig.6)** are more plannar than that of low confinement **(Fig.5)**, which is attributed to the higher confinement/ductility stabilizing the fracture propagation (lower K_{HF}).

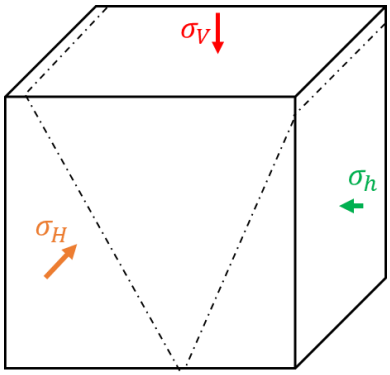

Fig.9 The failure mode of brittle materials under true triaxial stress compression i.e., $\sigma_v > \sigma_H > \sigma_h$ (Minaeian 2014; Rahjoo and Eberhardt 2021).

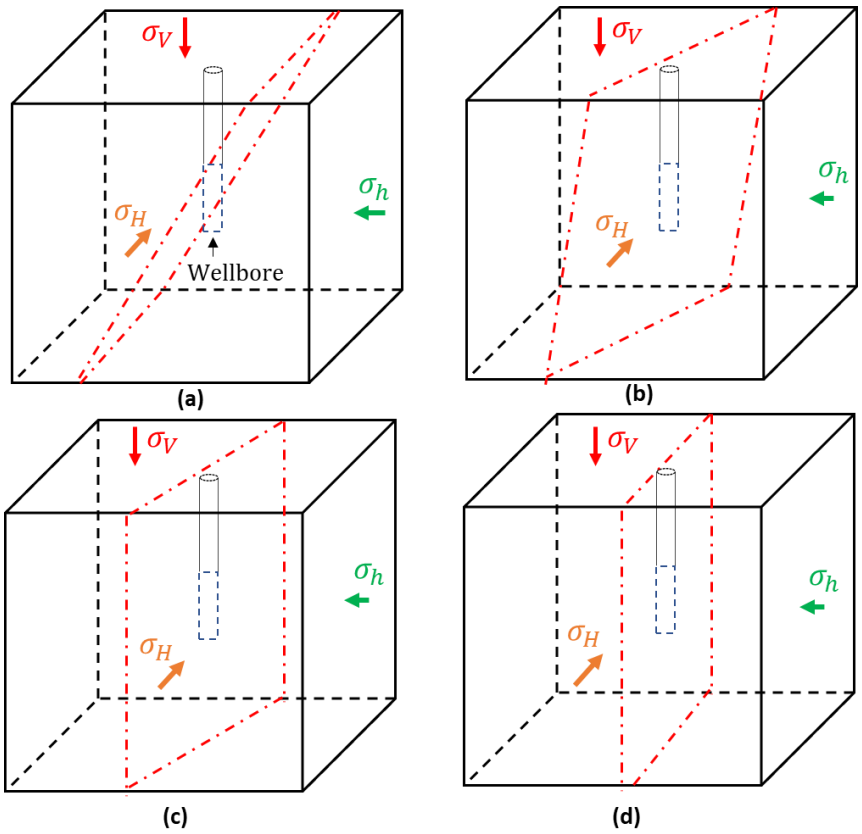

Fig.10 Representative Geometry of hydraulic fracture from brittle to ductile transition: **a)** brittle PMMA (under high confinement) **b)** brittle PMMA (under low confinement) or brittle/semi-brittle rock **c)** semi-ductile rock **d)** ductile rock. Note: the failure plane shown above is a simplified diagram, not necessarily indicating the fracture will exactly follow that plane or penetrated to the boundary of sample.

5.4 Role of BI in Fractured area

laboratory results indicated that the fractured area (A_{FN}) are reduced from brittle to ductile samples subjected to both low and high confinement (**Fig.11**), which is in good agreement with the numerical study recently performed by Ju et al. (2021). As shown in **Fig. 11**, the experimental results subjected to the high confinement (A_{FN} verse BI) shows an analogous polynomial relation comparing to the numerical results (A_{TN} verse BI); regardless of their quantities. For laboratory experiments, the limited sample size and continuously injected energy allow the fluid-driven fractures penetrate the boundary of sample; while the HF are retained within the boundary of numerical model due to the early termination of fracture propagation in ductile reservoirs (Ju et al. 2021).

Interestingly, for the same type of tested sample, the fractured area (A_{FN}) subjected to high confinement (15MPa, 10 MPa, and 5MPa) are larger than that of lower confinement (6.5MPa, 3 MPa, and 1.5MPa) (**Fig.11)**, although the brittleness index (BI) of former one is reduced. This could be attributed to: (i) higher deviatoric horizontal stress exerted on the samples

subjected to high confinement (Van Dam and De Pater 1999; Van Dam et al. 2000). (ii) higher stress concentration near the fracture tip due to the higher breakdown/propagation pressure. This coupled mechanism causes the fracture to propagate in a manner of relatively higher effective stress and sufficient propagating time, resulting in a more tortuous fracture with relatively rougher surface in the view of meso-scale (**Fig.12**).

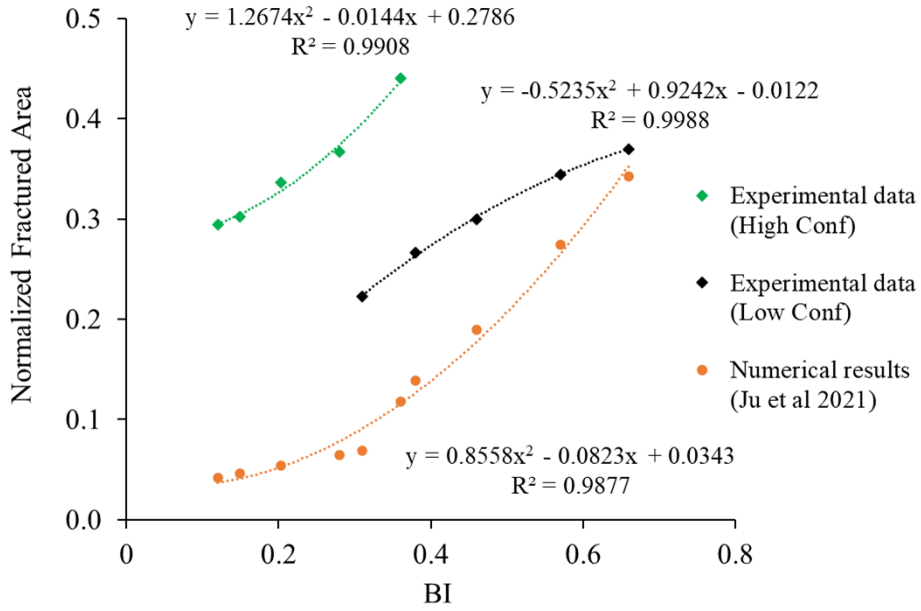

Fig.11 Normalized fractured area vs brittleness index (BI) based on our experimental results and literature data

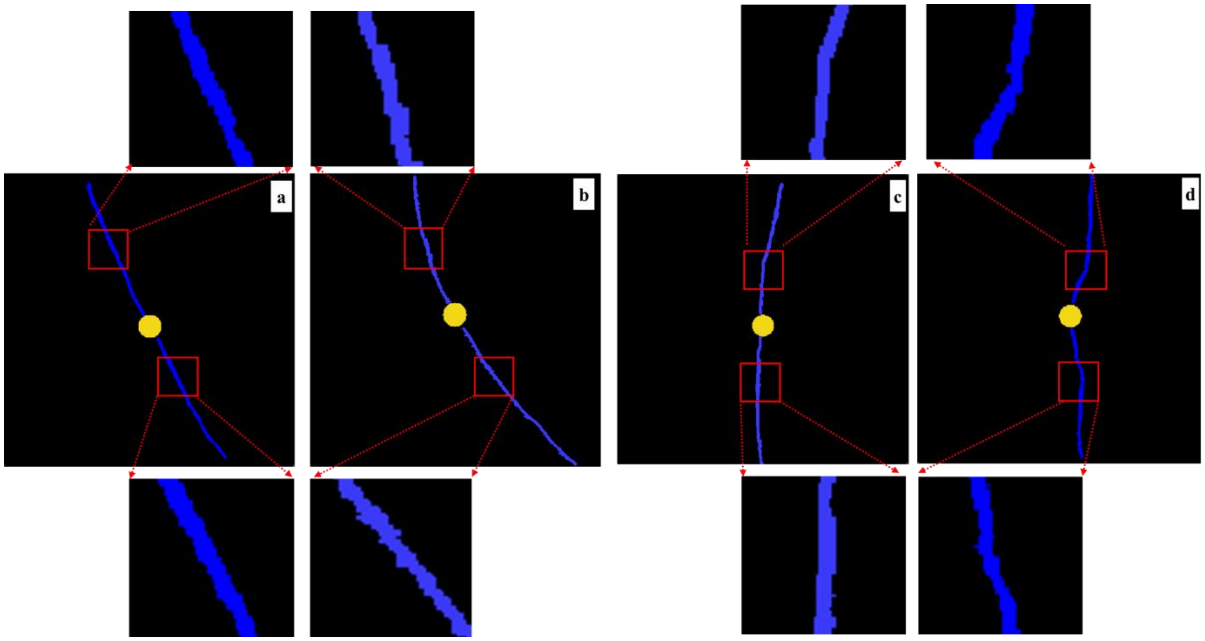

Fig.12 CT images of hydraulic fracture in semi-brittle rock S_1 under a) low and a) high confinement; ductile rock S_2 under c) low and d) high confinement

6. Conclusion

The initiation and propagation of hydraulic fractures in geomaterials plays an important role in geology (Weinberg and Regenauer-Lieb 2010), reservoir stimulation (Mandal et al. 2020; Bakhshi et al. 2021; Huang and Chen 2021) and the management of micro-seismicity (Amitrano 2003). However, the brittle-to-ductile transition with depth of the hydraulic fracturing process has been rarely quantified in the laboratory despite its pivotal role for benchmarking field operations.

In this study, we conducted hydraulic fracturing experiments on five types of rock samples in addition to PMMA, which represents the extreme brittle reference. The samples were subjected to true triaxial stress conditions (TTSC), and during fluid injection wellbore pressure and the three-dimensional (3D) strains induced by hydraulic fracture propagation were simultaneously monitored. After each experiment, the fractured sample was imaged using X-ray Computed Tomography (XCT); the 3D images were used to quantitatively evaluate the morphology and area of the induced hydraulic fracture (Avizo software). These experiments are designed to shed light on the hydraulic fracturing response as a function of depth for a wide range of engineering applications.

The interpretation of the hydro-mechanical data reveals that:

(i) The non-localized deformation induced by hydraulic fracturing in a semi-brittle sample (e.g., S_4), a semi-ductile sample (e.g., S_3), and a ductile sample (e.g., S_5 and S_2) are significantly enhanced at higher confinement (mean compressive stress) (**Figs.B1and B2**). However, for the extremely brittle PMMA (**Figs.B1a and b)**, and the semi-brittle sample S_1 (**Figs.B2a and b),** the failure is dominated by localized shear-dilation at both low and high confinement.

(ii) For a normal faulting regime (i.e., $\sigma_v > \sigma_H > \sigma_h$), the intermediate strain ε_H transists from tensile deflection to positive compression when transiting from a brittle to a ductile regime (**Fig.4)**; and this phenomenon is enhanced as the increase of confinement.

The transitional inclined angle (high-to-low) of HFs are observed from brittle/semi-brittle samples to semi-ductile/ductile samples:

(i) For the extremely brittle PMMA under high confinement, extremely high stress concentration near the crack tip leads to a strong hydro-shearing fracture (see **Figs.6a or 10a**), consistent with a normal faulting regime **(Fig.9)**.

(ii) For the semi-brittle samples (S_1 and S_4), the moderate plastic softening reduces the stress concentration at the fracture tip, inhibiting vertical hydro- shearing, but promoting horizontal hydro-dilating fractures (see **Figs.6b and c; Figs.10b and c**).

(iii) For the semi-ductile sample S_3 and the ductile samples (S_5 and S_2), the significant plastic softening behaviour at the fracture tip (Feng et al. 2020; Ju et al. 2021; Papanastasiou 1997; Parisio et al. 2021) reduces the near-tip stress concentration, which significantly reduces the effective propagation energy, allowing stress redistribution within the ductile rock surrounding the tip. This mechanism is thought to be the cause of the highly mitigated inclination of hydraulic fractures observed in samples S_3 (**Figs.5d and 6d; Fig.10c**) and S_5 (**Figs.5e and 6e; Fig.10c**), which contrasts with the fracture induced in sample S_2, i.e., nearly perpendicular to the minimum horizontal stress (**Figs.5f and 6f; Fig.10d**).

The correlation between normalized fractured area (A_{FN}) and brittleness index (BI) indicates that:

(i) The measured surface area of the hydraulic fractures is reduced when transiting from the brittle to the ductile regime, regardless of the confinement (**Fig 11**), which is in good agreement with the numerical study reported by Ju et al. (2021).

(ii) Notably, for the same type of sample under high confinement (15MPa, 10 MPa, and 5MPa), the fractured area (A_{FN}) is shown to be larger than that for lower confinement values (6.5MPa, 3 MPa, and 1.5MPa), despite the fact that the brittleness index (BI) is significantly reduced when confinement is significantly higher. This is attributed to a more tortuous fracture with a relatively rougher surface at high confinement (**Fig 12**).

Declaration of competing interest

The authors declare that they have no known competing interest

Acknowledgments

The first author sincerely thanks China Scholarship Council- Curtin International Postgraduate Research Scholarship (CSC-CIPRS, Grant No. 201808190001) for their financial support on this research.

Appendix A: Test Materials and Mechanical properties

Synthetic rock blocks constituted of variable fractions of fine-grain quartz, kaolinite clay, calcite, and Standard Portland cement mixture (**Table A1**) are moulded. The PMMA were additionally used as an ideally homogeneous and brittle reference. More details on the

fabrication procedures of block samples can be found in Sarmadivaleh and Rasouli (2015) and Feng et al. (2020). The prepared cubic/cylindrical blocks and the schematic of cubic sample assembly for a typical hydraulic fracturing test are shown in **Fig.A1**. In field, defects and stress concentrations play a role in hydraulic fracture propagating in mix-modes, i.e., non-perpendicular to the minimum principal stress (Parisio et al. 2021). To allow the stress concentration generating around the borehole, we design for drilling a 2/3 depth of the borehole (Feng et al. 2020; Parisio et al. 2021) (**Fig.A1**).The mechanical properties of prepared blocks are shown in **Table A2**. Details of the procedures for UCS and TCS testing used to determine these values can be found in Feng et al. (2020).

Table A1. Composition and density of the five synthetic rock formulations (mineral cement mixtures) used in this study.

Mineral-cement mixture	Silica (%)	Kaolinite (%)	Calcite (%)	Cement (%)	Density(g/cm³)
Quartz-rich(S_1)	52.5%	22.5%	0.0%	25%	1.58
Clay-rich(S_2)	22.5%	52.5%	0.0%	25%	1.26
Calcite-rich(S_3)	15.0%	7.5%	52.5%	25%	1.44
Mixed average(S_4)	30.0%	22.5%	22.5%	25%	1.50
Clay-rich$_2$(S_5)	30.0%	45%	0.0%	25%	1.46

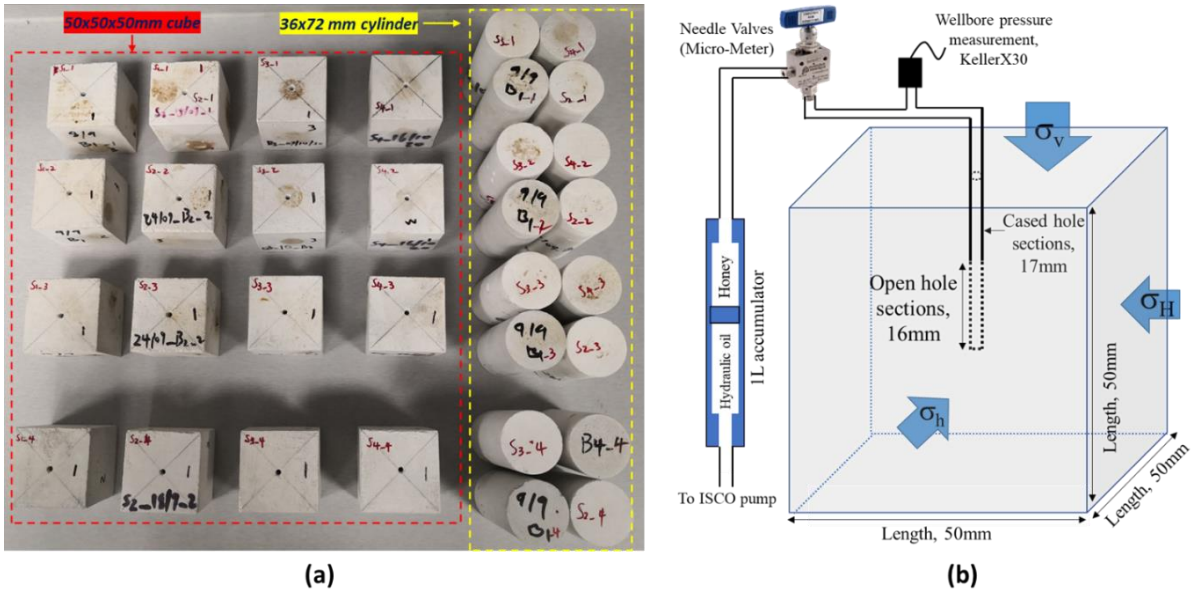

Fig.A1 a) Part of the synthetic rock samples used in this study: a) 50x50x50mm cubes for hydraulic fracturing, and 36x72mm cylindrical plugs for mechanical characterisation; b) schematic of a typical cubic sample prepared for hydraulic fracturing tests (modified from Feng et al. (2021)).

Table A2. Mechanical properties of the mineral-cement mixtures and PMMA used in this study, and determined through unconfined (UCS) and triaxial (TCS) compression tests.

Mineral-cement mixture	Young's modulus E (GPa)	Poisson's ratio ν (-)	Friction angle Φ (°)	Cohesion C_O (MPa)	P-wave velocity V_P (km/s)	S-wave velocity V_S (km/s)	Porosity ϕ (-)
Quartz-rich(S_1)	6.9*	0.17*	42*	1.76*	2.1	1.4	0.29
Clay-rich(S_2)	2.6*	0.1*	35.3*	0.6*	1.3	0.87	0.3
Calcite-rich(S_3)	3.2*	0.21*	40.9*	0.9*	1.69	1.07	0.2
Mixed average(S_4)	3.0*	0.18*	35.8*	1.5*	1.8	1.17	0.24
Clay-rich2(S_5)	1.6*	0.17*	37.3*	0.8*	1.47	0.97	0.3
PMMA(S_6)	6.2**	0.39**	14.4**	44.6**	2.75	1.4	0

** UCS tests are conducted on dry samples, and TCS tests are conducted in dry conditions at 0.6, 2.1, and 3.4 MPa confining pressure.*
*** Data reported in the literature.*

Appendix B: Full hydromechanical data set

Fig.B1 shows the acquired hydro-mechanical data set during the hydraulic fracturing from brittle to ductile samples under lower confinement (i.e., 6.5MPa , 3MPa, and 1.5MPa). As shown in **Fig.B1**, after formation breakdown (maximum wellbore pressure), the drop of BHP is initially accelerated then decelerated to the propagation pressure, the acceleration is displayed by the black dash arrow (linear), while the deceleration is displayed by blue dash arrow (nonlinear). For brittle failure in PMMA, the wellbore pressure dramatically drops from breakdown pressure to constant propagation pressure within a few seconds. For semi-brittle rock S_1 up to the constant propagation pressure, the acceleration of BHP drop takes major portion; while for the semi-brittle rock S_4, semi-ductile rock S_3, the partition of acceleration/deceleration are nearly equivalent. However, for ductile samples (S_5 and S_2), the acceleration only occupies a small portion, while the deceleration of BHP drop is major.

The minimum horizontal strain ε_h are induced by the initiation and propagation of the fracture (negative ε_h in green), whereas the positive strain ε_V along the vertical stress σ_V (blue curve) indicates the vertical shortening induced by the imposed vertical stress (except for PMMA where the ε_V is relatively constant). It revealed that the magnitude of strain ε_H along the intermediate horizontal stress σ_H (orange curve) show significantly tensile deflection for brittle PMMA2 (**Fig.B1a**) and S_1 (**Fig. B1b)** , or the semi-brittle rock S_4 (**Fig. B1c**); slightly tensile deflection for semi-ductile S_3 (**Fig. B1d**); but relatively constant ε_H for ductile sample S_5 (**Fig. B1e**). Noteworthy, the only slightly positive ε_H is observed for ductile sample S_2 (**Fig. B1f**). If we consider the fracture initiates where the pressurization rate starts to decrease, for the brittle PMMA **(Fig. B1a)**, semi-brittle rock S_1 **(Fig. B1b)** , and S_4 **(Fig. B1c)**, and semi-ductile rock S_3 **(Fig. B1d)**, there are significant portion where the 3D strain i.e. ε_V , ε_H, and ε_h are relatively constant before deflecting. However, for the very ductile samples (S_5 and S_2), limited strain are

kept as constant but quickly response after fracture initiation (**Figs. B1e and f**), especially for the very ductile sample S_2 (**Fig. B1f**).

Fig.B2 shows the hydro-mechanical data set acquired during the hydraulic fracturing from brittle to ductile sample under high confinement condition (i.e., 15MPa, 10MPa, and 5MPa). As shown in **Fig. B2**, the breakdown pressure (P_b) of PMMA shows the highest-4300psi, then for S_1 2500psi, while for the S_4, S_3, S_5 the P_b are relatively consistent (around 2000psi), and the lowest P_b is observed in S_2 (1500psi).For all samples after formation breakdown, the drop of BHP is only accelerated for a very short period but quickly turns to be decelerated. It is interesting to observe that even for the higher breakdown pressure (2500 psi) of S_1, the depressurization rate (DR) is lower(-6psi/s) than that of S_4 and S_3 (-10psi/s). The lowest depressurization rate (-2.5psi/s) is observed in S_2 and S_5 (-4psi/s). In terms of the 3D strain induced by hydraulic fracture propagation under higher stresses, for brittle PMMA4 (**Fig. B2a**) and S_1 **(Fig. B2b)**, or semi-brittle rock S_4 (**Fig. B2c**), the magnitude of intermediate horizontal strain ε_H (orange curve) is slightly tensile (negative) deflected, while the significant compressive deflection are observed for semi-ductile S_3 (**Fig. B2d**); ductile sample S_5 and S_2 (**Fig. B2e and f**).

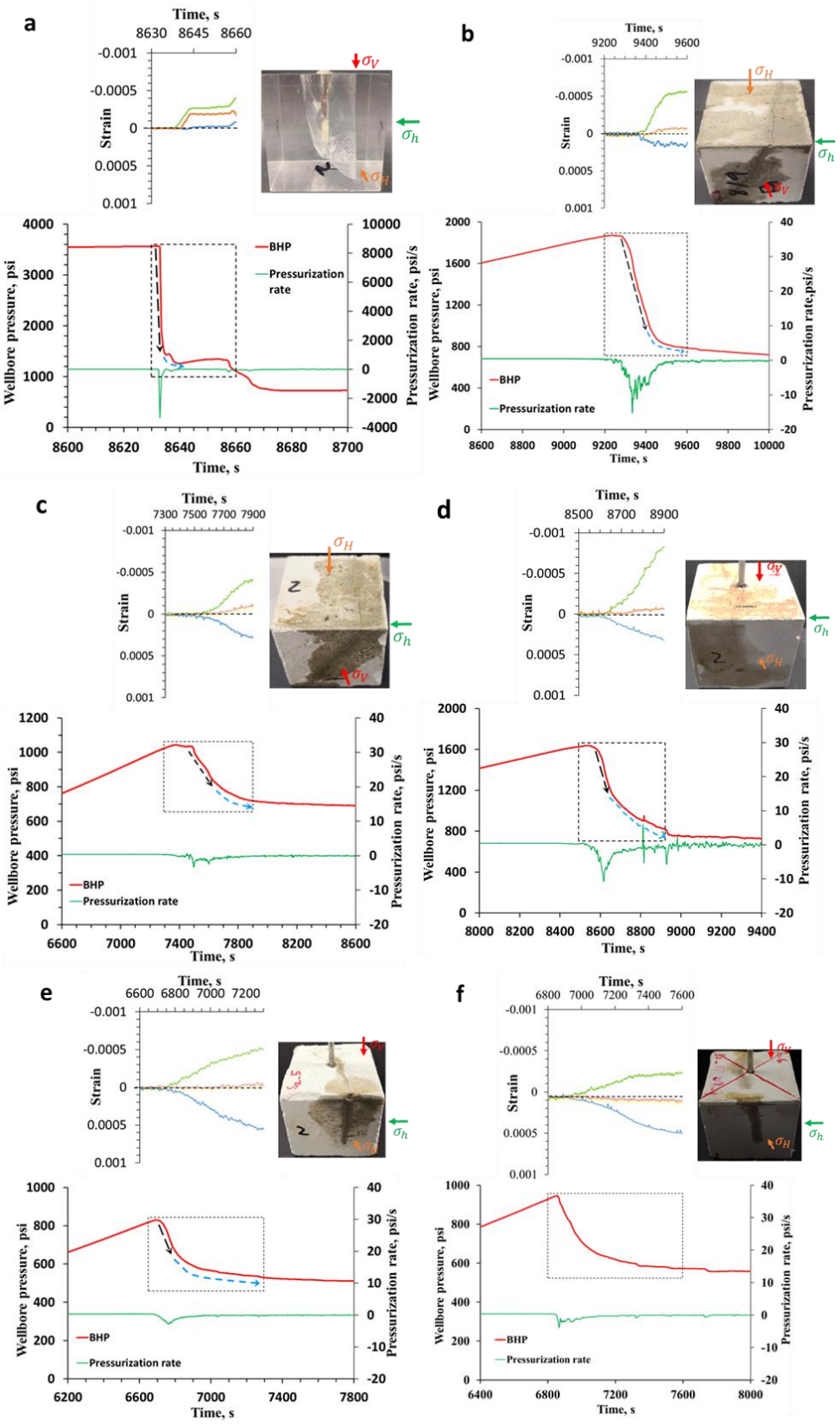

Fig.B1 Synchronization of wellbore pressure and hydraulic fracture induced strain under low confinement(6.5MPa , 3MPa, and 1.5MPa): a) PMMA2 b) S_1 c) S_4 d) S_3 e) S_5 f) S_2. Black dash arrow indicates the acceleration of pressure drop; Blue dash arrow indicates the deceleration of pressure drop. Black solid arrow indicates the time for starting of strain response; The tested samples are shown at the right top.

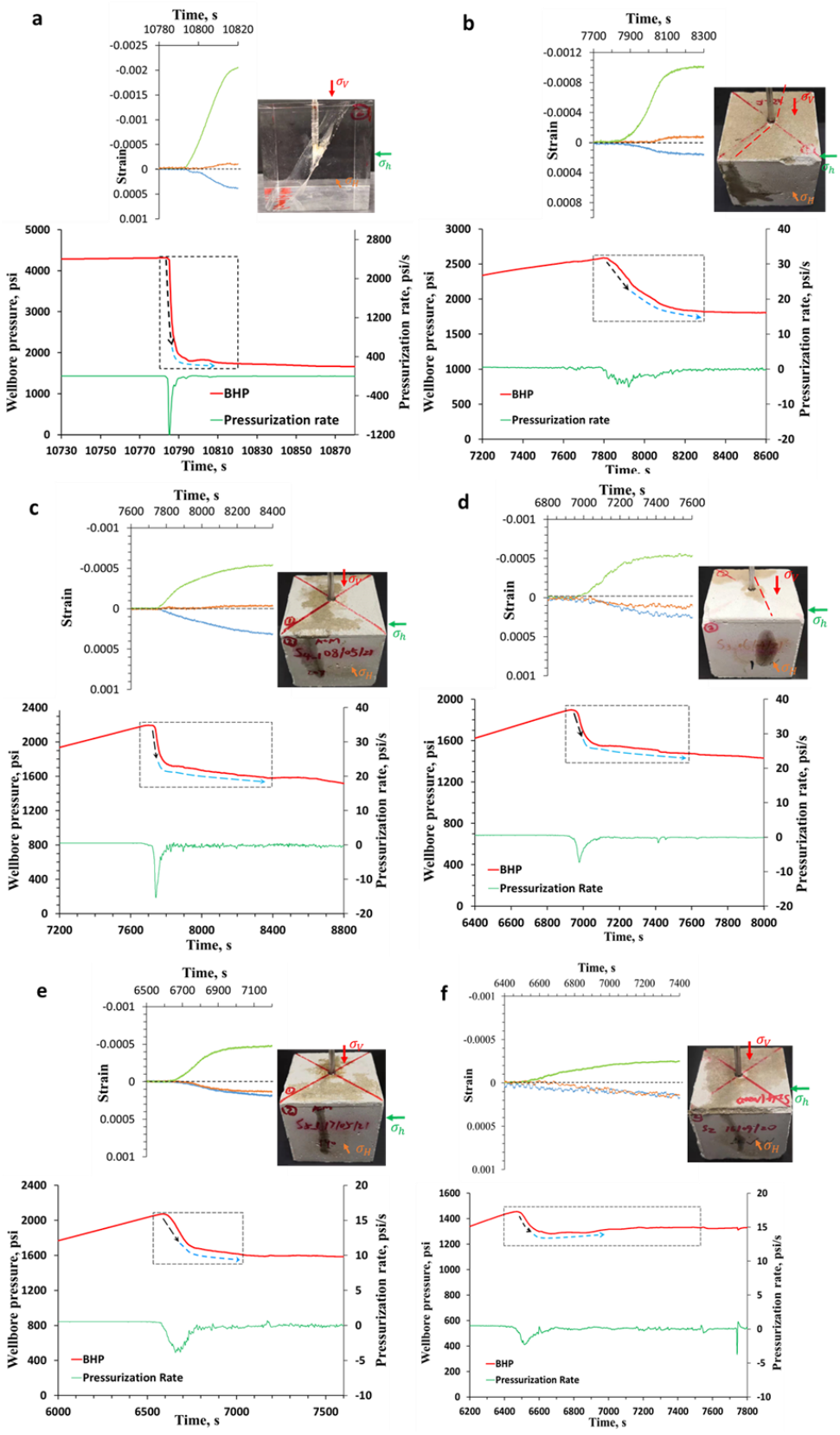

Fig.B2 Synchronization of wellbore pressure and hydraulic fracture induced strain under high confinement (15MPa , 10MPa, and 5MPa): a) PMMA4 b) S_1 c) S_4 d) S_3 e) S_5 f) S_2. Black dash arrow indicates the acceleration of pressure drop; Blue dash arrow indicates the deceleration of pressure drop. Black solid arrow indicates the time for starting of strain response; The tested samples are shown at the right top.

Reference

Aharonov E, Scholz CH (2019) The brittle-ductile transition predicted by a physics-based friction law. Journal of Geophysical Research: Solid Earth 124:2721-2737

Amitrano D (2003) Brittle-ductile transition and associated seismicity: Experimental and numerical studies and relationship with the b value. Journal of Geophysical Research: Solid Earth 108

Bakhshi E, Golsanami N, Chen L (2021) Numerical modeling and lattice method for characterizing hydraulic fracture propagation: a review of the numerical, experimental, and field studies. Archives of Computational Methods in Engineering 28:3329-3360

Barenblatt GI (1962) The mathematical theory of equilibrium cracks in brittle fracture. Advances in applied mechanics 7:55-129

Boone T, Wawrzynek P, Ingraffea A Simulation of the fracture process in rock with application to hydrofracturing. In: International Journal of Rock Mechanics and Mining Sciences & Geomechanics Abstracts, 1986. vol 3. Elsevier, pp 255-265

Bunger AP (2005) Near-surface hydraulic fracture. University of Minnesota,

Desroches J, Detournay E, Lenoach B, Papanastasiou P, Pearson JRA, Thiercelin M, Cheng A (1994) The crack tip region in hydraulic fracturing. Proceedings of the Royal Society of London Series A: Mathematical and Physical Sciences 447:39-48

Dugdale DS (1960) Yielding of steel sheets containing slits. Journal of the Mechanics and Physics of Solids 8:100-104

Economides MJ, Nolte KG (1989) Reservoir stimulation vol 2. Prentice Hall Englewood Cliffs, NJ,

Elices M, Guinea G, Gomez J, Planas J (2002) The cohesive zone model: advantages, limitations and challenges. Engineering fracture mechanics 69:137-163

Evans B, Fredrich JT, Wong TF (1990) The brittle-ductile transition in rocks: Recent experimental and theoretical progress The Brittle-Ductile Transition in Rocks, Geophys Monogr Ser 56:1-20

Feng R, Zhang Y, Rezagholilou A, Roshan H, Sarmadivaleh M (2020) Brittleness Index: from conventional to hydraulic fracturing energy model. Rock Mechanics and Rock Engineering 53:739-753

Feng R., Sarout J., Daustriat J., Ghuwainim Y., Rezaee R., Sarmadivaleh M (2022). Laboratory validation of a new hydro-mechanical energy-based brittleness index model for hydraulic fracturing. *International Journal of Rock Mechanics and Mining Science*, under review

Garagash DI (2019) Cohesive-zone effects in hydraulic fracture propagation. Journal of the Mechanics and Physics of Solids 133:103727

Gischig VS, Preisig G Hydro-fracturing versus hydro-shearing: a critical assessment of two distinct reservoir stimulation mechanisms. In: 13th ISRM International Congress of Rock Mechanics, 2015. OnePetro,

Hillerborg A, Modéer M, Petersson P-E (1976) Analysis of crack formation and crack growth in concrete by means of fracture mechanics and finite elements. Cement and concrete research 6:773-781

Huang C, Chen S (2021) Effects of Ductility of Organic-Rich Shale on Hydraulic Fracturing: A Fully Coupled Extended-Finite-Element-Method Analysis Using a Modified Cohesive Zone Model. SPE Journal 26:591-609

Irwin GR (1957) Analysis of stresses and strains near the end of a crack traversing a plate

Ju Y, Wu G, Wang Y, Liu P, Yang Y (2021) 3D Numerical Model for Hydraulic Fracture Propagation in Tight Ductile Reservoirs, Considering Multiple Influencing Factors via the Entropy Weight Method. SPE Journal:1-18

Keer L, Luk V, Freedman J (1977) Circumferential edge crack in a cylindrical cavity

Lhomme T (2005) Initiation of hydraulic fractures in natural sandstones

Li JX, Rezaee R, Müller TM (2020) Wettability effect on wave propagation in saturated porous medium. The Journal of the Acoustical Society of America 147:911-920

Liu D, Lecampion B (2021) Propagation of a plane-strain hydraulic fracture accounting for a rough cohesive zone. Journal of the Mechanics and Physics of Solids 149:104322

Liu Y et al. (2020) Mechanical properties and failure behavior of dry and water-saturated anisotropic coal under true-triaxial loading conditions.Rock Mechanics and Rock Engineering 53:4799-4818

Liu S., Klaus T., Feng R., Bona A., Sarmadivaleh M (2022). Microstructure-based Modelling of Hydraulic Fracturing in Low-Permeability Rocks using the Cohesive Element Method. *Rock Mechanics and Rock Engineering*, under review

Mandal PP, Sarout J, Rezaee R (2020) Geomechanical appraisal and prospectivity analysis of the Goldwyer shale accounting for stress variation and formation anisotropy. International Journal of Rock Mechanics and Mining Sciences 135:104513

Minaeian V (2014) True triaxial testing of sandstones and shales. Curtin University

Nilson R, Proffer W (1984) Engineering formulas for fractures emanating from cylindrical and spherical holes

Nygård R, Gutierrez M, Bratli RK, Høeg K (2006) Brittle–ductile transition, shear failure and leakage in shales and mudrocks. Marine and Petroleum Geology 23:201-212

Papanastasiou P (1997) The influence of plasticity in hydraulic fracturing. International Journal of Fracture 84:61-79
Papanastasiou P, Thiercelin M Influence of inelastic rock behaviour in hydraulic fracturing. In: International journal of rock mechanics and mining sciences & geomechanics abstracts, 1993. vol 7. Elsevier, pp 1241-1247
Parisio F et al. (2021) A laboratory study of hydraulic fracturing at the brittle-ductile transition. Scientific Reports 11:1-16
Rahjoo M, Eberhardt E (2021) Development of a 3-D confinement-dependent dilation model for brittle rocks; Part 1, derivation of a Cartesian plastic strain increments ratios approach for non-potential flow rules. International Journal of Rock Mechanics and Mining Sciences 145:104668
Richard D, Lerner E, Bouchbinder E (2021) Brittle to ductile transitions in glasses: Roles of soft defects and loading geometry. arXiv preprint arXiv:210305258
Sarmadivaleh M (2012) Experimental and numerical study of interaction of a pre-existing natural interface and an induced hydraulic fracture. Curtin University
Sarmadivaleh M, Rasouli V (2015) Test design and sample preparation procedure for experimental investigation of hydraulic fracturing interaction modes.Rock Mechanics and Rock Engineering 48:93-105
Vachaparampil A, Ghassemi A (2017) Failure characteristics of three shales under true-triaxial compression. International Journal of Rock Mechanics and Mining Sciences 100:151-159
Van Dam D, De Pater C Roughness of hydraulic fractures: The importance of in-situ stress and tip processes. In: SPE Annual Technical Conference and Exhibition, 1999. OnePetro,
Van Dam D, De Pater C, Romijn R (2000) Analysis of hydraulic fracture closure in laboratory experiments. SPE Production & Facilities 15:151-158
Wang H (2019) Hydraulic fracture propagation in naturally fractured reservoirs: Complex fracture or fracture networks. Journal of Natural Gas Science and Engineering 68:102911
Wang S, Sloan S, Fityus S, Griffiths D, Tang C (2013) Numerical modeling of pore pressure influence on fracture evolution in brittle heterogeneous rocks.Rock mechanics and rock engineering 46:1165-1182
Weinberg RF, Regenauer-Lieb K (2010) Ductile fractures and magma migration from source. Geology 38:363-366
Wong T-f, Baud P (2012) The brittle-ductile transition in porous rock: A review. Journal of Structural Geology 44:25-53
Wu R (2006) Some fundamental mechanisms of hydraulic fracturing. Georgia Institute of Technology,
Yang Y, Liu S, Chang X (2021) Fracture stiffness evaluation with waterless cryogenic treatment and its implication in fluid flowability of treated coals. International Journal of Rock Mechanics and Mining Sciences 142:104727
Zeng L, Reid N, Lu Y, Hossain MM, Saeedi A, Xie Q (2020) Effect of the fluid–shale interaction on salinity: implications for high-salinity flowback water during hydraulic fracturing in shales. Energy & Fuels 34:3031-3040
Zhang J, Davis DM, Wong T-F (1993) The brittle-ductile transition in porous sedimentary rocks: Geological implications for accretionary wedge aseismicity. Journal of Structural Geology 15:819-830
Zhang X, Jeffrey RG, Thiercelin M (2009) Mechanics of fluid-driven fracture growth in naturally fractured reservoirs with simple network geometries. Journal of Geophysical Research: Solid Earth 114
Zhou J, Chen M, Jin Y, Zhang G-q (2008) Analysis of fracture propagation behavior and fracture geometry using a tri-axial fracturing system in naturally fractured reservoirs. International Journal of Rock Mechanics and Mining Sciences 45:1143-1152